JCI The Journal of Clinical Investigation

Endothelial SRF/MRTF ablation causes vascular disease phenotypes in murine retinae

Christine Weinl, … , Ralf H. Adams, Alfred Nordheim

J Clin Invest. 2013;123(5):2193-2206. https://doi.org/10.1172/JCI64201.

Research Article **Vascular biology**

Retinal vessel homeostasis ensures normal ocular functions. Consequently, retinal hypovascularization and neovascularization, causing a lack and an excess of vessels, respectively, are hallmarks of human retinal pathology. We provide evidence that EC-specific genetic ablation of either the transcription factor SRF or its cofactors MRTF-A and MRTF-B, but not the SRF cofactors ELK1 or ELK4, cause retinal hypovascularization in the postnatal mouse eye. Inducible, EC-specific deficiency of SRF or MRTF-A/MRTF-B during postnatal angiogenesis impaired endothelial tip cell filopodia protrusion, resulting in incomplete formation of the retinal primary vascular plexus, absence of the deep plexi, and persistence of hyaloid vessels. All of these features are typical of human hypovascularization-related vitreoretinopathies, such as familial exudative vitreoretinopathies including Norrie disease. In contrast, conditional EC deletion of *Srf* in adult murine vessels elicited intraretinal neovascularization that was reminiscent of the age-related human pathologies retinal angiomatous proliferation and macular telangiectasia. These results indicate that angiogenic homeostasis is ensured by differential stage-specific functions of SRF target gene products in the developing versus the mature retinal vasculature and suggest that the actin-directed MRTF-SRF signaling axis could serve as a therapeutic target in the treatment of human vascular retinal diseases.

Endothelial SRF/MRTF ablation causes vascular disease phenotypes in murine retinae

Christine Weinl,[1] Heidemarie Riehle,[1] Dongjeong Park,[1] Christine Stritt,[1] Susanne Beck,[2] Gesine Huber,[2] Hartwig Wolburg,[3] Eric N. Olson,[4] Mathias W. Seeliger,[2] Ralf H. Adams,[5] and Alfred Nordheim[1]

[1]Department for Molecular Biology, Interfaculty Institute of Cell Biology, [2]Division of Ocular Neurodegeneration, Centre for Ophthalmology, Institute for Ophthalmic Research, and [3]Department of Pathology and Neuropathology, University of Tübingen, Tübingen, Germany. [4]Department of Molecular Biology, University of Texas Southwestern Medical Center, Dallas, Texas, USA. [5]Department of Tissue Morphogenesis, Max-Planck-Institute for Molecular Biomedicine, and Faculty of Medicine, University of Münster, Münster, Germany.

Retinal vessel homeostasis ensures normal ocular functions. Consequently, retinal hypovascularization and neovascularization, causing a lack and an excess of vessels, respectively, are hallmarks of human retinal pathology. We provide evidence that EC-specific genetic ablation of either the transcription factor SRF or its cofactors MRTF-A and MRTF-B, but not the SRF cofactors ELK1 or ELK4, cause retinal hypovascularization in the postnatal mouse eye. Inducible, EC-specific deficiency of SRF or MRTF-A/MRTF-B during postnatal angiogenesis impaired endothelial tip cell filopodia protrusion, resulting in incomplete formation of the retinal primary vascular plexus, absence of the deep plexi, and persistence of hyaloid vessels. All of these features are typical of human hypovascularization-related vitreoretinopathies, such as familial exudative vitreoretinopathies including Norrie disease. In contrast, conditional EC deletion of *Srf* in adult murine vessels elicited intraretinal neovascularization that was reminiscent of the age-related human pathologies retinal angiomatous proliferation and macular telangiectasia. These results indicate that angiogenic homeostasis is ensured by differential stage-specific functions of SRF target gene products in the developing versus the mature retinal vasculature and suggest that the actin-directed MRTF-SRF signaling axis could serve as a therapeutic target in the treatment of human vascular retinal diseases.

Introduction

Angiogenesis, the extension of preexisting vascular networks by EC proliferation and sprouting, is essential for organ development and organ function in health and disease (1, 2). Retinal capillary dysfunction, caused by either impaired vascular growth (hypovascularization) or excessive vascularization (hypervascularization or neoangiogenesis), leads to severe visual impairment and, often, blinding ocular diseases. Ocular hypovascularization diseases encompass familial exudative vitreoretinopathy (FEVR), including Norrie disease (ND) (3). Vessel hyperproliferation, associated with neovascularization (NV), is found in infants with retinopathy of prematurity (ROP) (4), in diabetic retinopathy (DR) (5), and in NV age-related macular degeneration (AMD) (6). NV AMD, which represents approximately 10% of all AMD yet accounts for nearly 90% of all AMD-associated vision losses (6), displays either choroidal NV or, more rarely, intraretinal NV. The latter is found in the manifestations of retinal angiomatous proliferation (RAP) (7) and macular telangiectasia (MacTel) (8–10).

During angiogenesis and EC sprouting, highly polarized ECs, termed tip cells, are positioned at the distal end of vessels. Stalk cells form the sprout base and maintain a continuous, lumenized connection to the existing vessel network (11). EC sprouting is highly dynamic and requires rapid rearrangements of the actin cytoskeleton (12). To sense VEGF gradients and other signals, tip cells continuously extend and retract filopodia and constantly compete with stalk cells for the leading position within angiogenic sprouts (13).

Murine postnatal retinal development offers insight into molecular and cellular mechanisms of angiogenesis. At P0, a ring-shaped vessel exists around the optic nerve head in the central retina, whereas peripheral regions lack vasculature. Angiogenic growth extends the retinal vasculature into the periphery, thereby establishing the 2-dimensional primary vessel plexus. In addition, beginning at approximately P8, perpendicular sprouting from the primary plexus leads to the formation of 2 additional vessel layers in the deeper retina, the deep plexi (14). Since global inactivation of genes controlling blood vessel morphogenesis often causes embryonic lethality, the development of inducible genetic models is highly important for the characterization of molecular pathways contributing to retinal angiogenesis in postnatal and adult stages (15).

Serum response factor (SRF) (16), a ubiquitously expressed transcription factor, regulates target gene expression in cell type–selective and signal-specific fashion upon recruitment of different cofactors (17). The SRF cofactors of the ternary complex factor family (TCFs; encoded by *Elk1*, *Elk3*, and *Elk4*) (18, 19) enable SRF-mediated induction of immediate-early genes (IEGs) upon Ras/MAPK signaling, whereas myocardin-related transcription factors (MRTFs; encoded by *Mrtfa* and *Mrtfb*, also known as *Mkl1* and *Mkl2*, respectively) (20–22) function as SRF cofactors responsive to Rho signaling and actin dynamics (23, 24) to regulate cytoskeletal genes (17, 25, 26). SRF binds a conserved target gene *cis* element, the CArG box [$CC(A/T)_6GG$] (17). Tissue-specific deletion of *Srf* revealed essential requirements for SRF activity in

Conflict of interest: The authors have declared that no conflict of interest exists.
Citation for this article: *J Clin Invest.* 2013;123(5):2193–2206. doi:10.1172/JCI64201.

many cell types, including muscle cells, neurons, and ECs (26). Dynamic rearrangements of the actin cytoskeleton are communicated to the genome by actin-directed cytoplasmic release of MRTF proteins, followed by induced nuclear MRTF-SRF interaction and activation of transcriptional responses (17, 23, 27). The contributions of SRF and its cofactors to EC function are poorly understood. In cultured ECs, ELK3 participates in transcriptional responses to hypoxia by regulation of HIF-1α protein stability (28, 29). In vitro cultured ECs revealed a role for SRF in VEGF-mediated angiogenesis, actin polymerization, and EC migration (30). The effects of VEGF on SRF activity were suggested to require both MAPK/Erk and RhoA signaling. In vivo, EC SRF loss-of-function studies were so far only performed during embryogenesis (31, 32), revealing a requirement for SRF in embryonic vascularization. Defects in actin polymerization and in EC intercellular junction formation resulted in embryonic death around E14.5 (31, 32). The genes encoding VEGF-R2 (*Kdr*; also known as *Vegfr2* or *Flk1*) and VE-cadherin (*Cdh5*), among others, were identified as SRF target genes stimulated upon VEGF signaling (31).

To overcome embryonic lethality of previously used genetic models (31, 32), we used mice expressing the tamoxifen-inducible recombinase *CreER^{T2}* under the control of the EC-specific *Cdh5* promoter (33), thus permitting temporally controlled deletion of floxed *Srf* and *Mrtf* genes in the endothelium. Postnatal EC ablation of either SRF or MRTFs led to severe developmental vessel growth defects, resembling major characteristics of inherited human retinal pathologies such as ROP and FEVR, including ND (3). Interestingly, we found that EC-specific deletion of *Srf* in adult mice triggered unwarranted intraretinal NV, reminiscent of the human NV AMD subtypes RAP and MacTel (7, 10), as well as the RAP/MacTel animal model deficient for the VLDL receptor (VLDLR; encoded by *Vldlr*) (9). Moreover, our study investigated EC VEGF signaling mechanisms in vitro and identified MRTF-SRF activation downstream of VEGF. Thus, the present findings offer new insight into the molecular and genetic basis of normal and pathological retinal angiogenesis and suggest cytoskeletal dynamics and the MRTF-SRF module as novel target structures for both diagnosis and treatment of human retinal vascular diseases.

Results

Lethality upon induced EC deletion of Srf during embryonic development. To validate a new genetic model for temporally controlled, induced EC-specific KO of *Srf* (referred to herein as *Srf^{iECKO}*), *Cdh5(PAC)-CreER^{T2}* transgenics (33) were bred with mice carrying a floxed *Srf* allele (*Srf^{flex1}*; ref. 34). Tamoxifen was applied successively to pregnant females, and embryos were analyzed at E14.5 or E17.5. Genotypes of the obtained embryos were distributed according to Mendelian ratios. Whereas control embryos appeared normal, freshly isolated *Srf^{iECKO}* embryos showed severe internal hemorrhaging in the head, back, and limb regions (Supplemental Figure 1, A–H; supplemental material available online with this article; doi:10.1172/JCI64201DS1). E17.5 *Srf^{iECKO}* embryos were significantly reduced in weight compared with E14.5 *Srf^{iECKO}* embryos and uninduced controls (Supplemental Figure 1I). Levels of *Srf* mRNA and SRF protein in embryonic limb buds isolated from *Srf^{iECKO}* animals were significantly reduced compared with control littermates (Supplemental Figure 1, J–L). These timed *Srf* deletion experiments demonstrated that our novel tamoxifen-inducible, EC-specific genetic system fully reproduced phenotypes during embryogenesis, which were previously reported for noninducible gene targeting using different Cre drivers and independently generated floxed *Srf* alleles (31, 32).

Postnatal EC Srf deletion causes impaired retinal angiogenesis. Taking advantage of the tamoxifen-inducible, temporally controlled gene targeting strategy, we chose the retina to study the effects of EC-specific *Srf* deletion on postnatal angiogenesis. Newborn pups were successively injected with tamoxifen at P1–P4, and vascularization was analyzed on retinal flat-mounts. As early as P6, isolectin B4 (ILB4) staining of the retinal primary plexus showed a significant 29% reduction in the area covered by blood vessels and a significant 35% decrease in the number of branch points in *Srf^{iECKO}* animals compared with littermate controls (Figure 1, A–C). Abnormal tip cell morphology was evident in *Srf^{iECKO}* retinae, with mutant sprouts displaying short shafts as well as fewer and shorter distal filopodia (Figure 1, A and D–F). These data suggest an essential role of SRF in postnatal angiogenesis, especially regarding progression of the retinal angiogenic front, which depends upon actin-mediated tip cell filopodial dynamics (11).

To monitor Cre recombination, we combined the *Srf^{iECKO}* model with double-fluorescent *mTmG* Cre reporter alleles (35), which switch expression from membrane-targeted Tomato protein (red) to GFP (green) upon Cre activation. Newborn mice were injected at P1–P4, and retinal flat-mounts were analyzed at P8 (Figure 1G). In the absence of the reporter, no specific signals were detected in either the red or the green channel. In retinae of uninjected *Srf$^{flex1/flex1}$Cdh5(PAC)-CreER^{T2}mTmG* mice, all retinal cells showed ubiquitous red fluorescence, whereas no specific signal in the green channel was observed. This proved that the system was not leaky, and no unspecific recombination occurred in the absence of tamoxifen. In retinae of tamoxifen-injected *Srf$^{flex1/WT}$Cdh5(PAC)-CreER^{T2}mTmG* control animals, ECs changed their color to green, highlighting efficient Cre recombination in the endothelium and the expected normal vascularization of the retina for age P8. In contrast, vessel outgrowth in tamoxifen-injected *Srf$^{flex1/flex1}$Cdh5(PAC)-CreER^{T2}mTmG* mice was strongly impaired, as evidenced by the abnormal position of the angiogenic front formed by green fluorescent, recombined ECs (Figure 1G).

Development of deep vascular plexi in the retina requires SRF function. *Srf^{iECKO}* animals at age P10 contained large avascular zones in the peripheral retina (Figure 2A), indicative of impaired development of the primary plexus until late stages of retinal vascularization. In control littermates, the primary plexus had reached the retinal periphery and started to extend into deeper retinal layers to form the tertiary and secondary capillary networks of the deep plexi (Figure 2, A, C, E, and F). In contrast, *Srf^{iECKO}* animals showed a 29% reduction in retinal area covered by blood vessels (Figure 2B). Interestingly, at the angiogenic front, large clusters of tip cells without filopodia formed (referred to as distal microaneurysms), which were never observed in control animals (Figure 2C). Abnormal accumulation of ECs within these microaneurysms was evidenced by EM (Figure 2D). Despite the abnormal accumulation of ECs within distal microaneurysms, these abnormal vessel structures were covered by pericytes (Figure 2D). Additionally, deep plexi were not established in *Srf^{iECKO}* animals (most likely as a consequence of abnormal sprouting in the primary plexus), which was further evidenced by EM, whereas control retinae revealed normal deep plexi vessel structures (Figure 2, F and G). Notably, we did not find a reduction in EC proliferation in *Srf^{iECKO}* retinae compared with controls (data not shown).

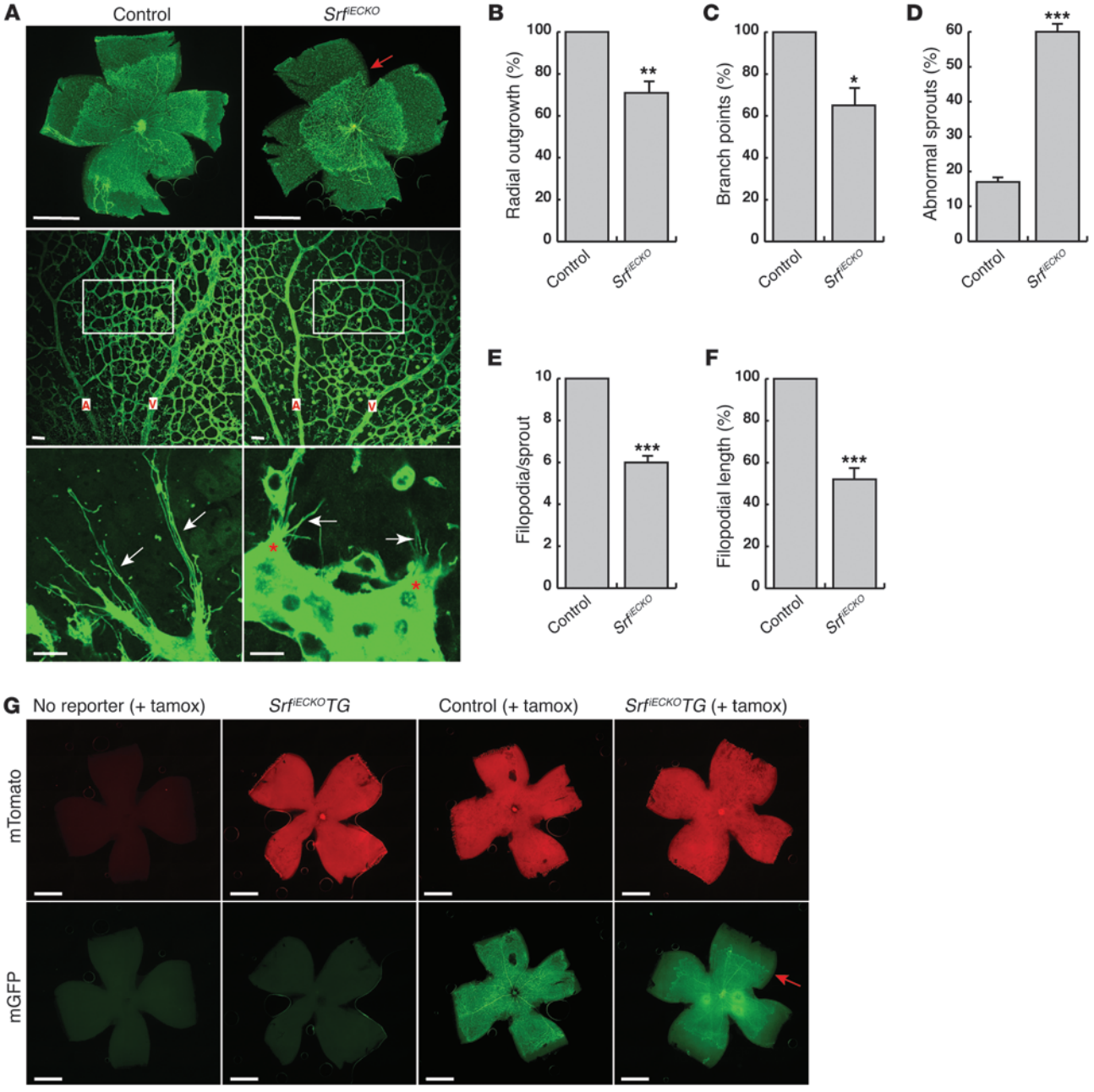

Figure 1

EC depletion of SRF impairs angiogenesis in P6 murine retinal development. (**A**) ILB4-stained retinal flat-mounts of P6 control and *Srf*^{iECKO} mice. Top: Progression of angiogenic front. Red arrow indicates recessed angiogenic front of the primary plexus in *Srf*^{iECKO} retinae. Images are composites (see Methods). Middle: Vessel density between artery (A) and vein (V). Bottom: Sprout morphology. White arrows indicate filopodia; red asterisks highlight abnormal morphologies of *Srf*^{iECKO} tip cells. (**B**) Quantitation of retinal area covered by blood vessels (radial outgrowth), expressed as percentage of control. $n = 6$ retinae. (**C** and **D**) Quantitation of (**C**) branch points in a field of view (**A**, middle, white boxes) and (**D**) abnormal sprouts. $n = 4$ retinae. (**E** and **F**) Quantitation of (**E**) filopodial number per sprout and (**F**) mean length of individual filopodia. $n = 30$ sprouts (control); 39 sprouts (*Srf*^{iECKO}). (**G**) Retinal flat-mounts of P8 mice lacking the double-fluorescent *mTmG* Cre reporter, *Srf*$^{flex1/flex1}$*Cdh5(PAC)-CreER*^{T2} *mTmG* mice (*Srf*^{iECKO}*TG*), and control *Srf*$^{flex1/WT}$*Cdh5(PAC)-CreER*^{T2}*mTmG* mice. Shown are red fluorescent channel (mTomato) and GFP (mGFP) signals of the same retinae, the latter being obtained upon *CreER*^{T2} activation by intragastric tamoxifen injection (+ tamox). Red arrow indicates recessed angiogenic front of the primary plexus in *Srf*$^{flex1/flex1}$*Cdh5(PAC)-CreER*^{T2}*mTmG* retinae. Images are composites (see Methods). Scale bars: 1 mm (**A**, top, and **G**); 50 μm (**A**, middle); 15 μm (**A**, bottom). $^{*}P < 0.05$, $^{**}P < 0.01$, $^{***}P < 0.001$ vs. respective control.

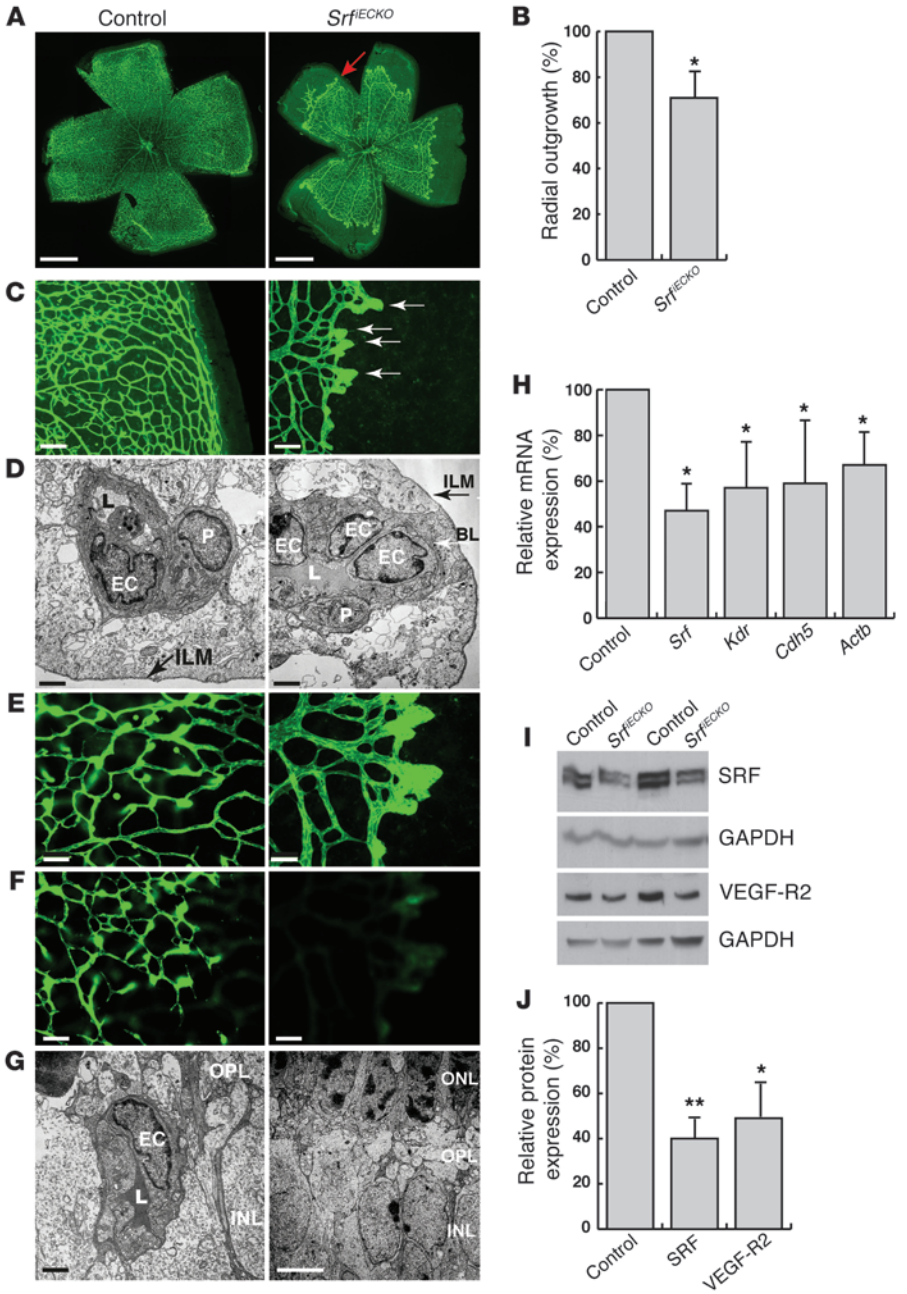

Figure 2

Avascular zones, distal microaneurysms, and lack of deep plexi in Srf^{iECKO} retinae at P10. (**A**) ILB4-stained retinal flat-mounts. Red arrow indicates recessed angiogenic front in the Srf^{iECKO} primary plexus. Images are composites (see Methods). (**B**) Radial outgrowth, expressed as percent of control. n = 19 retinae (control); 9 retinae (Srf^{iECKO}). (**C**) Higher magnification of ILB4-stained retinal flat-mounts. White arrows indicate microaneurysms in Srf^{iECKO} retinae. (**D**) EM image of blood vessels near the inner limiting membrane (ILM) to visualize the primary plexus. P, pericyte; L, lumen; BL, basal lamina. (**E** and **F**) ILB4-stained retinal capillaries of (**E**) the primary plexus and (**F**) deep plexi, which revealed complete absence of deeper capillaries in Srf^{iECKO} retinae. (**G**) EM image visualizing deep plexi. OPL, outer plexiform layer. (**H**) Semiquantitative RT-PCR of mRNA expression in purified ECs of P10 retinae. n = 4 (*Srf*); 3 (*Kdr* and *Actb*); 5 (*Cdh5*). mRNA levels were normalized to *Gapdh* and expressed as percent of control. (**I**) Western blot analysis of 2 representative pairs of control and Srf^{iECKO} P10 whole retinal tissue. (**J**) Quantitation of Western blot. SRF (n = 5) and VEGF-R2 (n = 4) levels were normalized to GAPDH and expressed as percent of control. Scale bars: 1 mm (**A**), 100 μm (**C**), 2 μm (**D** and **G**, left), 50 μm (**E** and **F**), 5 μm (**G**, right). $^*P < 0.05$, $^{**}P < 0.01$ vs. respective control.

To quantitate SRF-mediated gene expression, ECs were enriched from retinal tissue of tamoxifen-treated control and Srf^{iECKO} P10 animals, using anti-CD31–coated magnetic beads. mRNA levels of *Srf*, as well as SRF target genes *Kdr*, *Cdh5*, and *Actb* (also known as β-*actin*), were significantly decreased in Srf^{iECKO} retinae (Figure 2H). Correspondingly, protein levels of SRF and VEGF-R2 in whole retinal tissue were reduced by 60% and 51%, respectively (Figure 2, I and J).

Persistence of vascular defects in Srf^{iECKO} retinae after postnatal deletion of Srf. Postnatal retinal angiogenesis of WT mice reaches completion by P25 (14). At advanced ages (P15–P31), retinal irregularities remained in Srf^{iECKO} animals: in vivo imaging using confocal scanning laser ophthalmoscopy (SLO), particularly in fluorescence angiography (FLA) mode, revealed persistent distal microaneurysms of different sizes (Figure 3A). Additionally, no deep plexi were detectable in FLA recordings in retinae of these older Srf^{iECKO} mice, and no significant leakage of fluorescent dye out of microaneurysms was observed. Distal microaneurysms were visualized at the persistently recessed angiogenic fronts upon ILB4 staining of retinal flat-mounts, performed after completion of the in vivo imaging (Figure 3B). Further vascular abnormalities in Srf^{iECKO} retinae were found in H&E stainings of ocular paraffin sections. Srf^{iECKO} retinae displayed distal microaneurysms positioned aberrantly in the inner nuclear layer (INL; Figure 3C). Prior to histological preparation, the identical, persistent abnormal blood vessels were detected in vivo via optical coherence tomography (OCT; Figure 3C). The punctate double reflectance patterns typical of vessels (dark zones at the top and bottom of each vessel) were clearly visible.

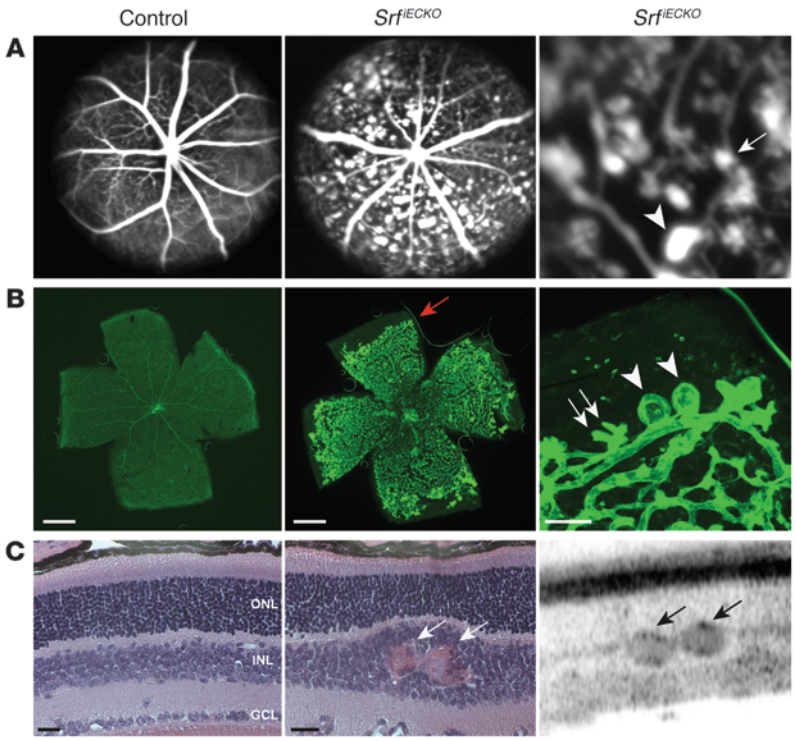

Figure 3
Vascular abnormalities in SRF-depleted retinae at P17. (**A**) SLO FLA of P17 control and *Srf*^{iECKO} mice. An enlarged view of the middle panel is shown at right (enlarged ×3-fold). (**B**) ILB4 staining on retinal flat-mounts after SLO imaging (flat-mount preparation included removal of hyaloid vessels). Images are composites (see Methods). Distal microaneurysms of different sizes (white arrows, small; arrowheads, large), as visualized in vivo in **A**, were also observed by ILB4 staining (see higher-magnification view at right). Red arrow indicates recessed angiogenic front of the primary plexus in *Srf*^{iECKO} retinae. (**C**) Visualization of microaneurysms in *Srf*^{iECKO} retinae by OCT (right) and, subsequently, by H&E staining of paraffin sections (left and middle). In *Srf*^{iECKO} retinae, erythrocyte-filled microaneurysms were present (white arrows) that caused local displacement of other layers. OCT confirmed this finding to be similarly identifiable in vivo in *Srf*^{iECKO} retinae (black arrows indicate distal microaneurysms). GCL, ganglion cell layer. Scale bars: 1 mm (**B**, left and middle); 100 μm (**B**, right); 25 μm (**C**).

SRF deficiency leads to defective hyaloid vessel regression. The presence of avascular zones in the periphery o *Srf*^{iECKO} retinae led us to test whether hyaloid vessels persist, as this vessel system, normally regressing during postnatal development, is known to be retained when the vascular network is compromised (36). Interestingly, in 64% (7 of 11) of *Srf*^{iECKO} retinae, persisting hyaloid vessels were seen on flat-mounts (Figure 4A). With the exception of 1 of the 10 animals analyzed, no hyaloid vessels were detected on control retinal flat-mounts (Figure 4A). Retinal flat-mounts of control animals revealed the existence of all capillary beds and vascularization into the periphery, whereas the presence of hyaloid vessels in *Srf*^{iECKO} retinae coincided with large avascular zones, microaneurysms, and the absence of deeper capillary beds (Figure 4A). In vivo, the course of hyaloid vessels retained in the *Srf*^{iECKO} retinae could be followed by SLO angiography examining different focal planes of the same eye: hyaloids rose up from their origin at the retinal center and moved toward the back of the lens, then down toward the avascular "target zone" in the periphery (Figure 4B). The functional status of these vessels was verified by visible blood flow and pulsations of the whole vessel, as detected by SLO in vivo (data not shown).

Molecular and structural defects in Srf^{iECKO} *retinal blood vessels*. Retinal blood vessels grow along an underlying astrocytic network, which presents a gradient of matrix-bound VEGF (36). We analyzed the structure of this astrocytic network by glial fibrillary acidic protein (GFAP) staining of P6 retinal flat-mounts. In both control and *Srf*^{iECKO} retinae, astrocytes had reached the periphery and formed elaborate networks (Figure 5A). Control EC sprouts followed the preceding astrocytic network in close overlap, whereas the overlap between distal vessels and astrocytes was markedly reduced in *Srf*^{iECKO} retinae (Figure 5A). Next, we tested whether the mutant phenotype was caused by sprout retraction and vessel collapse. Both events would generate empty collagen IV sleeves, which are no longer associated with ECs (37, 38). In control retinae, the overlap between EC ILB4 and collagen IV patterns was almost complete (Figure 5B). In *Srf*^{iECKO} flat-mounts, we focused on the distal microaneurysms at the angiogenic front, which revealed a complete absence of empty collagen sleeves (Figure 5B), indicating that retraction of sprouts or vessels was not the reason for the observed vascular defects.

SRF deficiency in neurons of the forebrain resulted in increased Ser3 phosphorylation of the actin-severing protein cofilin (39). To analyze whether this indicator of imbalance in actin dynamics was also evident in SRF-deficient retinal ECs, we performed phosphorylated cofilin (P-cofilin) staining on retinal flat-mounts. Low basal P-cofilin staining was detected on control retinal vessels, which was slightly stronger than the neuronal signal in the ganglion cell layer underneath (Figure 5C). In contrast, strong P-cofilin staining was found in distal microaneurysms of *Srf*^{iECKO} mutants (Figure 5C). In addition, we observed an increased P-cofilin signal in whole retinal tissue (Figure 5, D and E).

Adult Srf^{iECKO} *eyes display retinal NV reminiscent of the Vldlr*$^{-/-}$ *phenotype*. To examine whether SRF plays a role in the maintenance of the fully established mature retinal vasculature of adult mice, *Srf* deletion was induced at 4–6 weeks of age, well after the completion of all developmental growth and maturation processes. Resulting ocular phenotypes were analyzed by SLO, OCT, and staining on paraffin sections. Covering a time span of 3–26 weeks after adult-stage tamoxifen injection, 82% of *Srf*^{iECKO} animals (n = 11) displayed multiple ectopic intraretinal NVs that were not observed in control littermates, as shown by in vivo SLO followed by H&E staining after paraffin sectioning (Figure 6, A–D). The abnormal NV structures were further characterized in OCT (Figure 6A). Collectively, these analyses revealed that NV retinal capillaries originated from deep plexi and connected to the retinal pigment epithelium (RPE). At the site of connection, RPE cells appeared to engulf the NV. Additionally, local distortion of outer nuclear layer

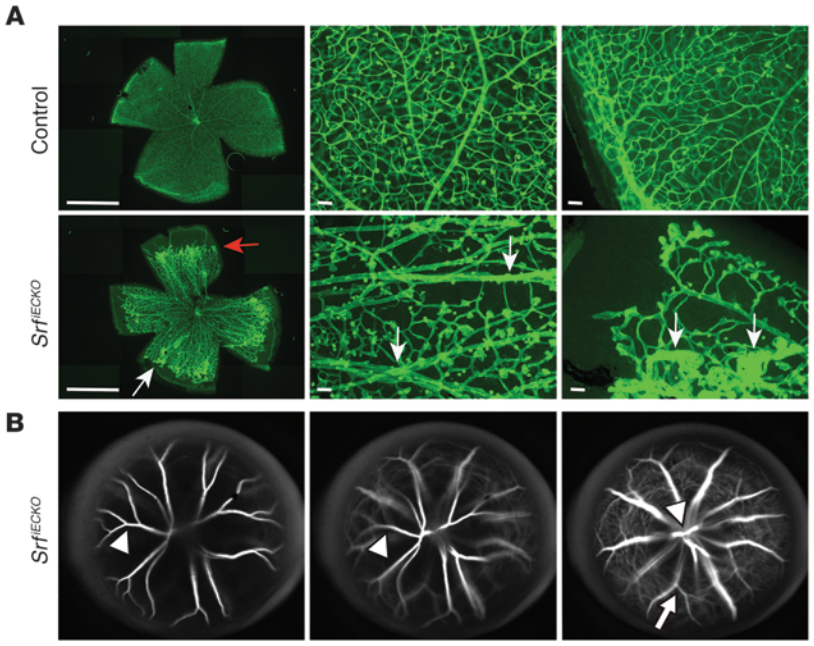

Figure 4
Impaired regression of hyaloid vessels in *Srf*^{iECKO} retinae. (**A**) ILB4 staining on retinal flat-mounts of P17 control and *Srf*^{iECKO} retinae, displayed at lower (left; composite images, see Methods) and higher (middle and right) magnification. Flat-mount preparation used conditions to preserve hyaloid vessels. Red arrow indicates retarded angiogenic front; white arrows indicate persistent hyaloid vessels in *Srf*^{iECKO} retinae. In the central area (middle), all capillary beds and no hyaloids were demonstrated in control retinae, whereas in *Srf*^{iECKO} retinae, deep plexi were absent, but hyaloids were present. In the periphery (right), control retinae demonstrated complete vascularization, whereas outer avascular zones remained in *Srf*^{iECKO} retinae, displaying distal microaneurysms and hyaloid vessels. (**B**) SLO angiography of *Srf*^{iECKO} eyes revealed the course of hyaloid vessels, from their origin at the retinal center toward the avascular "target zone" in the periphery, via tracing on 3 different focal planes of the same eye (right, retinal surface; middle, intermediate level; left, just below the lens). Arrowheads denote hyaloid vessels, arrow denotes retinal vessel. Scale bars: 1 mm (**A**, left); 100 μm (**A**, middle and right).

(ONL) and INL layering was evident in *Srf*^{iECKO} retinae (Figure 6D). We confirmed the intraretinal origin and endothelial nature of the NV lesions by ILB4 fluorescence staining (Figure 6E). Thus, formation of intraretinal NV clearly indicated that SRF function is critically required to maintain endothelial homeostasis of a healthy adult retinal vasculature.

The observed NV phenotype in adult *Srf*^{iECKO} retinae was highly reminiscent of that previously seen in *Vldlr*$^{-/-}$ retinae (9, 40–43), which also display intraretinal NV that is associated with photoreceptor degeneration. We therefore used 6- to 8-month-old *Srf*^{iECKO} and control littermates to analyze in further detail signs of retinal degeneration. Similar to *Vldlr*$^{-/-}$ retinae (9), we found multiple NV lesions with rupture of the RPE, RPE cells surrounding the NV site, mislayering and cell displacement within the INL and ONL, and thinning of the ONL in *Srf*^{iECKO} animals (Figure 7A). Semiquantitative RT-PCR of whole retinal tissue for cone-specific expression of *Opn1* (encoding opsin-1) and rod-specific expression of *Rho* (encoding rhodopsin), which are related to photoreceptor viability and health (9), revealed a significant 23% decrease in levels of both mRNAs in *Srf*^{iECKO} mice (Figure 7B). However, the mRNA level of *Vegfa* was unchanged in our model (Figure 7B), consistent with our earlier demonstration by in vivo SLO imaging of perfused, intact, and nonleaky blood vessels (Figure 6, B and C). In an attempt to uncover potential cellular mechanisms underlying the NV phenotype, we used an in vitro approach, downregulating SRF by siRNA in cultured immortalized mouse ECs (mECs) (44). Western blotting confirmed that SRF protein was downregulated after transfection of mECs with siRNA against *Srf* (Figure 7, C and D). The obtained decrease in *Srf* mRNA correlated with a decrease in the SRF target gene *Actb*, as assayed by semiquantitative RT-PCR. *Cfl1* (encoding cofilin) — which was previously found not to be under SRF transcriptional control, but rather posttranslational control (39) — was expectedly unchanged at the mRNA level (Figure 7E). However, most interestingly, mRNA expression of *Thbs1* (encoding the VLDLR ligand thrombospondin-1) was significantly decreased in SRF-depleted mECs (Figure 7E). The thrombospondin promoter contains a perfect SRF-binding CArG-box of CCTTATTTGG sequence at promoter coordinate –1.2 kb (45). Using ChIP, we showed that SRF bound to this element in the *Thbs1* gene; *Pak1*, a CArG box–negative locus, served as normalization control, and *Actb* served as positive reference (Figure 7F). Taken together, these results demonstrated that EC-specific ablation of SRF in the adult retinal endothelium leads to NV lesions associated with reduced photoreceptor viability. The congruence of this phenotype with *Vldlr*$^{-/-}$ mice, together with our finding that the VLDLR ligand thrombospondin-1 was under transcriptional control of SRF in mECs, suggests that impairment of the antiproliferative VLDLR-thrombospondin pathway contributes to formation of intraretinal NV lesions in adult *Srf*^{iECKO} retinae.

MRTF, but not TCF, cofactors are essential for retinal angiogenesis. To identify cofactors recruited by SRF in mediating retinal vascular development, we performed KO studies on 4 of the 5 known genes encoding TCFs and MRTFs. We first took advantage of a newly generated, constitutive *Elk1*$^{-/-}$*Elk4*$^{-/-}$ double-KO mouse model (46). In the retinal vasculature, radial outgrowth was found to be unaffected in P6 and P10 *Elk1*$^{-/-}$*Elk4*$^{-/-}$ versus controls, which included *Elk1*$^{-/-}$*Elk4*$^{+/+}$ and *Elk1*$^{-/-}$*Elk4*$^{+/-}$ genotypes (Figure 8, A, B, D, and E). The angiogenic front of *Elk1*$^{-/-}$*Elk4*$^{-/-}$ retinae at P6 appeared normal: tip cells extended numerous filopodia indistinguishable from those of controls (Figure 8C). Moreover, deep plexi were visible in both control and *Elk1*$^{-/-}$*Elk4*$^{-/-}$ retinae at P10 (Figure 8, F and G). SRF and P-cofilin protein levels were unchanged in *Elk1*$^{-/-}$*Elk4*$^{-/-}$ retinae (Supplemental Figure 2B). These data demonstrated that the TCF-type SRF cofactors ELK1 and ELK4 were not required for vascularization of the retina.

To determine whether the SRF cofactors MRTF-A and MRTF-B play a role in SRF-dependent retinal angiogenesis instead, we generated mice with *Cre*-inducible EC-specific KO of MRTF-B on a constitutive *Mrtfa*-KO background (referred to herein as *Mrtfa*$^{-/-}$*Mrtfb*^{iECKO} mice). *Mrtfa*$^{-/-}$*Mrtfb*^{iECKO} mice showed retinal blood vessel defects highly reminiscent of those of *Srf*^{iECKO} mice. This congruency in phenotype with *Srf*^{iECKO} mice was evidenced by the *Mrtfa*$^{-/-}$

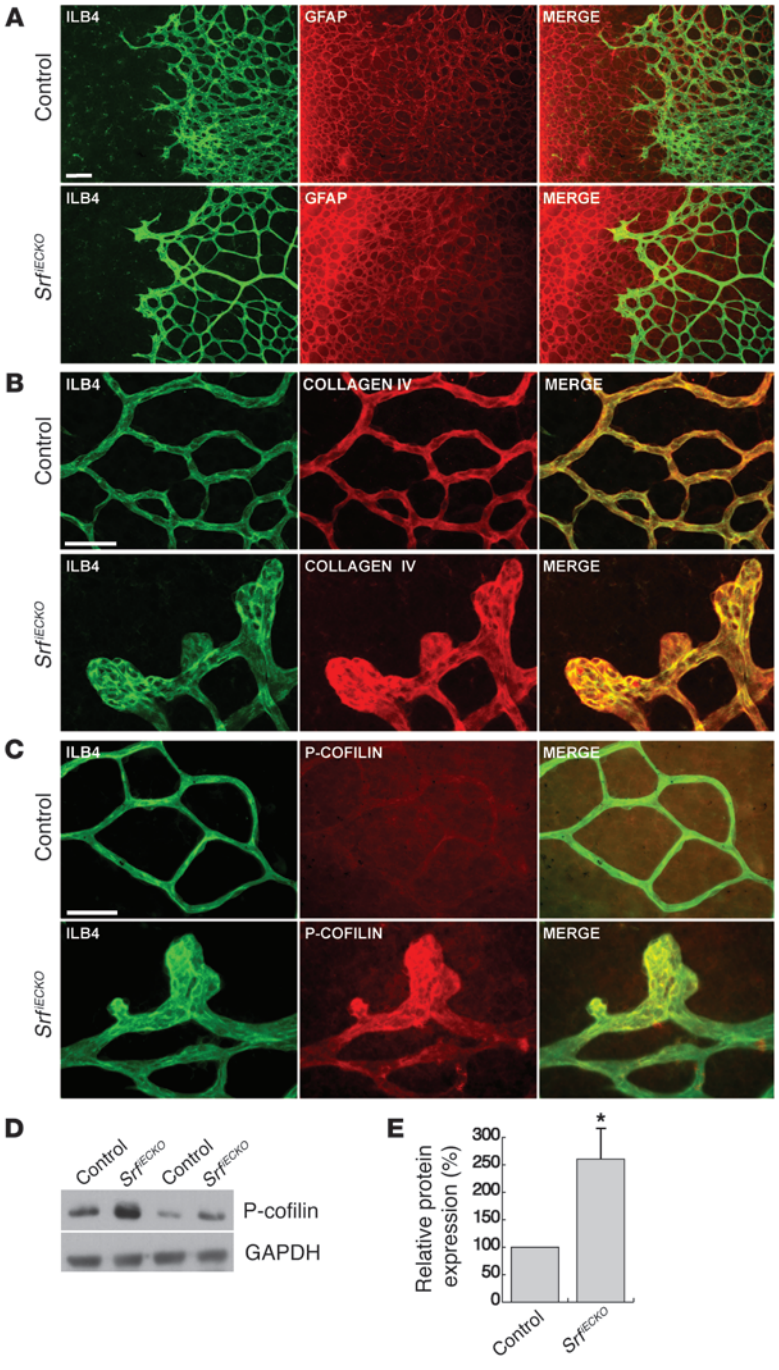

Figure 5

Srf^{iECKO} retinal capillaries grow on a normal astrocytic network, are covered by collagen IV, and display elevated P-cofilin in distal microaneurysms. (**A**) Retinal flat-mounts stained for ILB4 (green) and GFAP (red) of P6 control and *Srf*^{iECKO} mice. (**B**) Retinal flat-mounts stained for ILB4 (green) and collagen IV (red) of P10 control and *Srf*^{iECKO} mice. (**C**) Retinal flat-mounts stained for ILB4 (green) and P-cofilin (red) of P10 control and *Srf*^{iECKO} mice. (**D**) 2 representative pairs of control and *Srf*^{iECKO} whole–retinal tissue Western blots of P-cofilin. GAPDH served as loading control. (**E**) Western blot signals of P-cofilin from whole retinal tissue, expressed as percent of control. $n = 8$. Scale bar: 50 μm (**A**–**C**). $^*P < 0.05$ vs. respective control.

Mrtfb^{iECKO} animals' reductions in radial outgrowth at P6 and P10, number of branching points, formation of abnormal sprouts at P6, and formation of distal microaneurysms as well as by their absence of deep plexi at P10 (Figure 9, A–D and G–J). The reductions in filopodial number and length were comparable in *Mrtfa*$^{-/-}$*Mrtfb*^{iECKO} retinae (Figure 9, E and F) and in *Srf*^{iECKO} retinae. Importantly, in *Mrtfa*$^{-/-}$*Mrtfb*^{iECKO} retinae, SRF protein levels were unchanged, whereas P-cofilin was markedly increased (Supplemental Figure 2, A and B). KO of *Mrtfa* and *Mrtfb* individually caused partial impairment of angiogenic front progression in each genotype. Detailed analysis of radial outgrowth in P8 retinae suggested a gene-dosage effect: radial outgrowth decreased successively with decreasing WT allele composition for *Mrtfa* and *Mrtfb* (Figure 9K and Supplemental Figure 3). Taken together, the highly overlapping phenotypic characteristics of *Mrtfa*$^{-/-}$*Mrtfb*^{iECKO} and *Srf*^{iECKO} mice were strongly suggestive of MRTFs being the relevant EC SRF cofactors in vivo ensuring appropriate retinal angiogenesis.

VEGF-A induces cytoplasm-to-nucleus translocation of MRTF-A and SRF target gene expression. The above genetic evidence for essential contributions of SRF and MRTF to retinal angiogenesis led us to investigate signaling cascades activating SRF in mECs. Interestingly, both serum and VEGF-A treatment of mECs activated MRTF-A to translocate from the cytoplasm to the nucleus (Figure 10A). The sensitivity of this effect to latrunculin B (Figure 10A) suggested involvement of G-actin in retaining MRTF-A within the cytoplasm (24). Similarly, cytochalasin D and jasplakinolide, 2 F-actin–modulating substances known to liberate MRTF from G-actin (24, 27), induced nuclear MRTF-A translocation in mECs (Supplemental Figure 4). To further probe into the functionality of VEGF-induced MRTF activation, we used luciferase-based transient reporter gene assays, which harbored promoter sequences that either did $[(TSm)_2]$ or did not $[(Tmm)_2]$ contain an intact SRF binding site (Figure 10B). In transfected human retinal microvascular ECs (HRMECs), VEGF-stimulated $(TSm)_2$ reporter activity was enhanced by cotransfected MRTF expression vectors, an effect that was dependent on the presence of intact SRF binding sites (Figure 10C). Finally, VEGF-A treatment of mECs increased mRNA levels of the endogenous SRF target genes *Flt1* (also known as *Vegfr1*), *Kdr*, *Srf*, *Actb*, and *Fos* (Figure 10D). These results argue for VEGF-induced cooperation of SRF and MRTF in ECs that leads to expression of essential proangiogenic genes. We therefore propose that VEGF-induced MRTF translocation to the nucleus activates in ECs expression of SRF target genes with cytoskeletal functions, which in turn is essential for motile activities of tip cells to ensure appropriate vascularization of the postnatal retina (Figure 10E).

Discussion

The genetic study presented here identifies the murine transcription factor SRF to be essential for EC function, both during postnatal

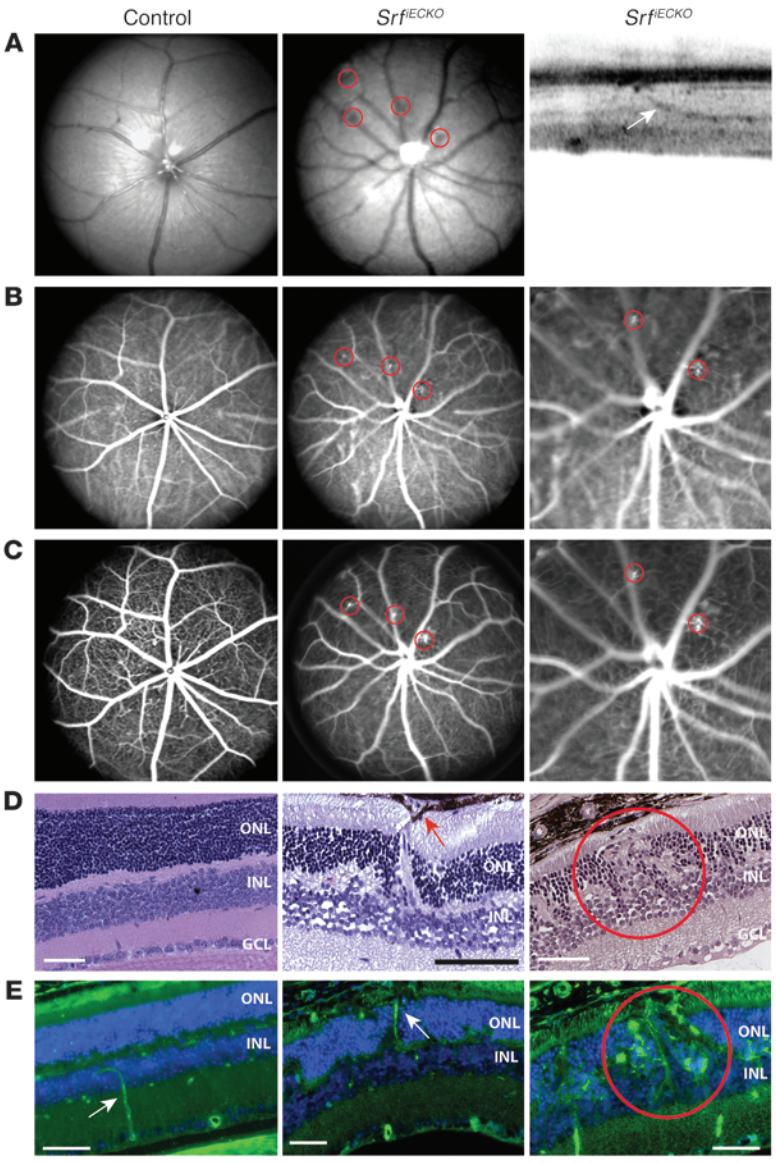

Figure 6
Retinal NV upon adult-induced SRF depletion. NV lesions are indicated by red circles. (**A**) Left and middle: Fundus imaging (514 nm) of control and *Srf*^{iECKO} adult animals. Right: OCT visualizing an intraretinal capillary targeting the RPE (white arrow). (**B** and **C**) ICG angiography (795 nm) to show retinal and choroidal vessels (**B**), and (**C**) FLA to enhance visibility of retinal vessels and capillaries, for control and *Srf*^{iECKO} adult animals. Higher-magnification views of 2 local NV structures in *Srf*^{iECKO} animals are shown at right (enlarged ×3-fold). (**D**) H&E staining on paraffin sections revealed normal layering in control eyes, but intraretinal NV structures in *Srf*^{iECKO} eyes, penetrating toward the RPE. Red arrow indicates RPE cells surrounding the NV sprout. (**E**) Fluorescent imaging of control and *Srf*^{iECKO} eyes on paraffin sections. EC staining with ILB4 (green) and cell nuclei (blue) in the subretinal space. White arrow indicates an ILB4-positive blood vessel. Scale bars: 50 μm (**D** and **E**).

development of the retinal vasculature and in maintenance of adult capillary homeostasis. Most importantly, whereas EC-specific SRF ablation at postnatal stages caused hypovascularization of the primary plexus and the absence of deep retinal plexi, EC depletion of SRF at adult stages led to intraretinal NV. Both of these opposing murine phenotypes, elicited upon stage-specific SRF depletion, resembled blinding human retinopathies, i.e., developmental hypovascularization found in early-onset FEVR (including ND) (3, 47) versus the adult-onset intraretinal NV AMD subtypes RAP and MacTel (7, 8).

Alterations of retinal vessels were the earliest phenotypic effects we detected upon induction of postnatal or adult EC-specific SRF depletion. However, besides the retinal phenotype, we observed some behavioral abnormalities. We attribute these behavioral effects to compromised functions of cerebral microvessels, which do not appear to exert influences on the retinal phenotype described here and will be characterized separately.

Postnatal defects in retinal development upon EC-specific *Srf* deletion included retarded progression of the angiogenic front and impaired tip cell filopodial protrusion, which generated avascular zones and distal microaneurysms in the primary plexus and, consequently, a complete absence of deep plexi. This was associated with persistence of the hyaloid vasculature. EC-specific depletion of the SRF cofactors MRTF-A/MRTF-B, but not ELK1/ELK4, led to similar phenotypes with respect to postnatal retinal vascularization, thereby providing clear genetic evidence for an essential functional interaction of SRF and MRTFs in directing EC activities. Since actin dynamics provide a driving force for such motility functions, including tip cell filopodial activity (11, 12), our observation that VEGF-A signaling elicited actin-dependent translocation of cytoplasmic MRTF into the nucleus represents a new molecular mechanism by which angiogenic signals induce motile functions of ECs.

The phenotype upon postnatal ablation of MRTF-SRF signaling described herein showed strong similarities to human pathologies and murine model systems of FEVR, including ND (47, 48). Since identified genetic lesions eliciting FEVR and ND fall into the Wnt signaling pathway, including mutant alleles for *Ndp*, *Fzd4*, *Lrp5*, and *Tspan12* (3), our data suggest the existence of cross-talk between Wnt and actin signaling in guaranteeing proper EC function during retinal angiogenesis.

In contrast to postnatal SRF depletion, *Srf* deletion in adult ECs elicited intraretinal NV. This phenotype was characterized by neoangiogenic activities originating from intraretinal deep capillaries and causing non–uniformly distributed focal lesions. The latter displayed distortions in INL and ONL layering, local thinning of the ONL, disruption of photoreceptors associated with reduced expression of *Opn1* and *Rho*, and rupture of the RPE with RPE cells enveloping the NV structures. Collectively, these abnormalities represent characteristic features of the human NV AMD subtypes RAP (7) and MacTel (8–10). Very similar phenotypic features were displayed by mice deficient for VLDLR, a component of reelin signaling exerting inhibitory effects on EC proliferation (9, 40–43). In addition to binding reelin, VLDLR also binds the ligand thrombospondin-1 (49, 50). The glycoprotein thrombos-

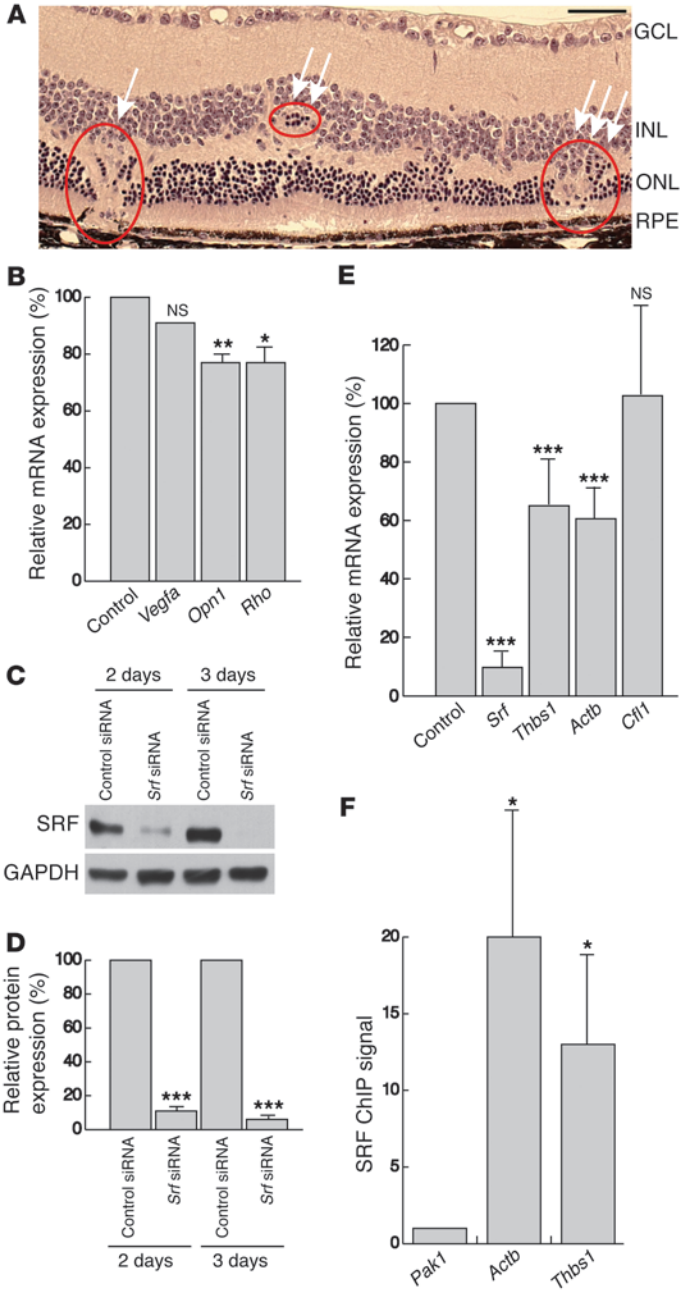

Figure 7

NV causes non–uniformly distributed focal lesions in adult SRF-depleted retinae and results in retinal mislayering and photoreceptor degeneration. (**A**) H&E staining on paraffin sections of Srf^{iECKO} eyes showed retinal abnormalities, including NV lesion connecting to and rupturing the RPE (arrow), local displacement of ONL cells (double arrow), and mislayering of INL and ONL and thinning of the ONL (triple arrow), accompanied by local disruption of photoreceptors. (**B**) Semiquantitative RT-PCR analysis of *Vegfa*, *Opn1*, and *Rho* mRNA expression of whole retinal tissue of 6- to 8-month-old control and Srf^{iECKO} animals. mRNA levels were normalized to *Gapdh* and expressed as percent of control. $n = 6$ per group. (**C**) Representative Western blot analysis of SRF levels in immortalized mECs transfected with control siRNA and siRNA against *Srf* for 2 or 3 days. GAPDH was used as a loading control. (**D**) Quantitation of Western blot analysis in **C**, normalized to GAPDH and expressed as percent of control siRNA. $n = 5$. (**E**) Semiquantitative RT-PCR analysis of *Srf*, *Thbs1*, *Actb*, and *Cfl1* mRNA expression in immortalized mECs after transfection with siRNA against *Srf* compared with transfection with control siRNA. mRNA levels were normalized to *Gapdh* and expressed as percent of control. $n = 5$ experiments. (**F**) Quantitation of anti-SRF ChIP signals for promoter regions of *Pak1* (CArG-box negative locus used as normalization control), *Actb* (positive reference), and *Thbs1*. $n = 5$. Scale bar: 50 μm (**A**). $^*P < 0.05$, $^{**}P < 0.01$, $^{***}P < 0.001$ vs. respective control.

pondin is an extracellular matrix component known to inhibit EC proliferation (51, 52). Interestingly, the *THBS1* gene has been previously suggested to be under transcriptional control of SRF in human fibroblasts (45). Using siRNA and ChIP approaches, we here provided evidence suggesting *Thbs1* expression is under control of SRF in cultured mECs (Figure 7). We therefore hypothesize that SRF-controlled expression of thrombospondin is required in adult retinal vessels to inhibit pathological EC proliferation, thereby providing an explanation for both the NV phenotype we observed upon adult-stage SRF depletion and the overlapping phenotypic characteristics with the MacTel model of $Vldlr^{-/-}$ mice. As shown in the $Vldlr^{-/-}$ model, constitutive VLDLR deficiency did not severely affect postnatal development of the primary plexus, but rather caused abnormal intraretinal vessel growth during deep plexi formation (9), which suggests that VLDLR functions in maintaining homeostasis of primarily deep retinal vessels. Our phenotype of intraretinal NV upon adult SRF depletion and the hypothesized impairment of VLDLR signaling by associated thrombospondin deficiency are fully consistent with the defects displayed by $Vldlr^{-/-}$ mice.

Both RAP and MacTel show age-dependent onset in human patients. Since SRF activities are known to deteriorate in some aging cells (53), it will be of great interest to explore potential contributions of age-dependent SRF activity changes in the aging retinal endothelium of human AMD patients. Furthermore, our work might suggest modulation of EC SRF activity, as well as elevation of thrombospondin activity, as therapeutic options for the treatment of some NV AMD pathologies, such as RAP and MacTel.

The MRTF/SRF transcriptional feedback circuit, which links cytoplasmic actin polymerization with nuclear gene regulation, represents one of the best-understood mechanisms for genomic sensing of cytoskeletal dynamics (24, 27). Associated cellular functions include dynamic changes regarding cell polarity, cell shape, migration, and guided growth, all of which are essential to EC biology. Mechanistically, our conclusion that VEGF-A signaling activates G-actin–dependent MRTF-A translocation from the cytoplasm to the nucleus (Figure 10E) positions the MRTF-SRF module at the center of angiogenic regulation.

In conclusion, our genetic study using conditional depletion of SRF and MRTFs provides the first in vivo identification of any function for these transcription factors in the retinal endothelium of living animals. The phenotypic defects we describe in postnatal and adult retinal angiogenesis provide new insight into both the molecular developmental biology of retinal angiogenesis and the etiology of selected retinal pathologies. The findings reported here may help to define therapeutic approaches for the treatment of some human diseases related to abnormal retinal vascularization.

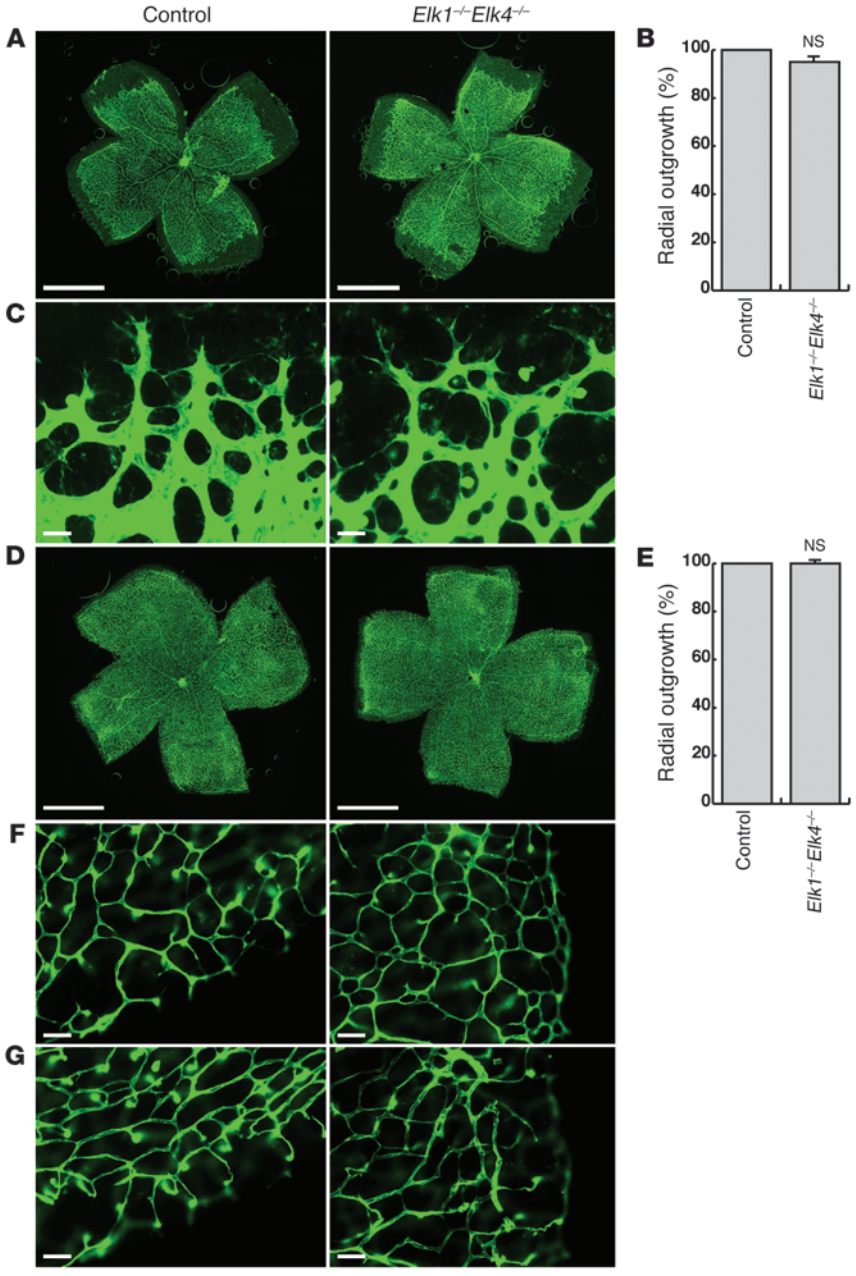

Figure 8
The TCF-type SRF cofactors ELK1 and ELK4 are not essential for normal retinal angiogenesis. (**A**) ILB4 staining on P6 control and *Elk1*$^{-/-}$*Elk4*$^{-/-}$ retinae. Images are composites (see Methods). (**B**) Quantitation of retinal area covered by blood vessels (percent radial outgrowth) at P6. n = 39 retinae (control); 20 retinae (*Elk1*$^{-/-}$*Elk4*$^{-/-}$). (**C**) Representative images of angiogenic fronts at P6. (**D**) ILB4 staining on P10 retinae. Images are composites (see Methods). (**E**) Percent radial outgrowth at P10. n = 10 retinae per group. (**F** and **G**) ILB4-stained retinal capillaries of (**F**) the primary plexus and (**G**) deep plexi at P10. Scale bars: 1 mm (**A** and **D**); 30 μm (**C**); 50 μm (**F** and **G**).

Methods

Animals. To generate KO mice with EC-specific SRF deletion (*Srf*^{iECKO} mice), female mice homozygous for the floxed *Srf*^{flex1} allele (34) were crossed with *Srf*$^{flex1/WT}$*Cdh5(PAC)-CreER*^{T2} male mice, which carry the *Cdh5(PAC)-CreER*^{T2} transgene (33). *Srf*$^{flex1/WT}$, *Srf*$^{flex1/flex1}$, and *Srf*$^{flex1/WT}$ *Cdh5(PAC)-CreER*^{T2} mice were used as controls. Double-KO *Elk1*$^{-/-}$*Elk4*$^{-/-}$ animals (provided by R. Treisman, Cancer Research UK, London, United Kingdom) were bred as described previously (46). Double-KO mice with EC-specific MRTF-B deletion (*Mrtfa*$^{-/-}$*Mrtfb*^{iECKO} mice) were generated by breeding the *Cdh5(PAC)-CreER*^{T2} transgene into *Mrtfa*$^{-/-}$*Mrtfb*$^{fl/fl}$ animals (25). Matings of *Mrtfa*$^{+/-}$*Mrtfb*$^{fl/fl}$ females with *Mrtfa*$^{-/-}$*Mrtfb*$^{fl/WT}$*Cdh5(PAC)-CreER*^{T2} males yielded the double-KO genotype *Mrtfa*$^{-/-}$*Mrtfb*$^{fl/fl}$*Cdh5(PAC)-CreER*^{T2}, and conditional deletion of the *Mrtfb*$^{fl/fl}$ alleles was induced by tamoxifen injection. To monitor Cre activity, mice carrying the *mTmG* double-fluorescent reporter (35) were crossed into the *Srf*^{flex1}*Cdh5(PAC)-CreER*^{T2} background. Genotyping was performed by PCR of tail biopsies (see Supplemental Table 1 for primer sequences).

Tamoxifen injections. For embryonic Cre activation, timed pregnant females were injected intraperitoneally on E10.5, E12.5, and E14.5 with 2 mg tamoxifen (dissolved in sunflower oil), and embryos were analyzed on E17.5. In a second series of experiments, females were injected on E10.5, E11.5, and E12.5, and embryos were analyzed on E14.5. For postnatal Cre activation, newborn pups were injected intragastrically on P1–P4 with 0.05 mg tamoxifen and analyzed on P6, P8, and P10 and at advanced age (P15–P31). For adult analysis, 4- to 6-week-old mice were injected intraperitoneally with 2 mg tamoxifen on 5 consecutive days and analyzed at different time points, ranging from 3 to 26 weeks after the last injection.

Antibody staining of retinal flat-mounts. Eyes were isolated and fixed in 4% PFA for 2 hours (54). After washing 2× for 5 minutes with PBS, retinae were dissected and incubated in blocking buffer (1% BSA, 0.3% Triton-X, and PBS) overnight at 4°C. After washing 3× for 5 minutes with PBS, retinae were treated 3× for 20 minutes with Pblec buffer (1 mM $CaCl_2$, 1 mM $MgCl_2$, 0.1 mM $MnCl_2$, 1% Triton-X, and PBS, pH 6.8). Incubation with primary antibodies was done at 4°C in Pblec buffer overnight. After washing 3× for 20 minutes with half blocking solution (0.5% BSA, 0.15% Triton-X, and PBS), retinae were incubated with secondary antibodies (2 hours at room temperature). After washing 3× for 20 minutes in half blocking solution, retinae were flat-mounted on coverslides and embedded in Mowiol.

Primary antibodies were as follows: ILB4 from *Griffonia simplificolia* (1:25 dilution; Sigma-Aldrich); GFAP (1:100 dilution; DAKO); collagen IV (1:40 dilution; AbD Serotec); P-cofilin (1:100 dilution; Cell Signaling). Secondary antibodies (all from Molecular Probes) were as follows: streptavidin–Alexa Fluor 488 (1:100 dilution), anti-rabbit Alexa Fluor 546 (1:200 dilution), anti-rat Alexa Fluor 546 (1:200 dilution).

Analysis of morphometric parameters of retinal flat-mounts. Radial outgrowth was determined as the ratio of blood vessel–covered retinal area to total retinal area, and expressed as a percentage. Branch points were counted

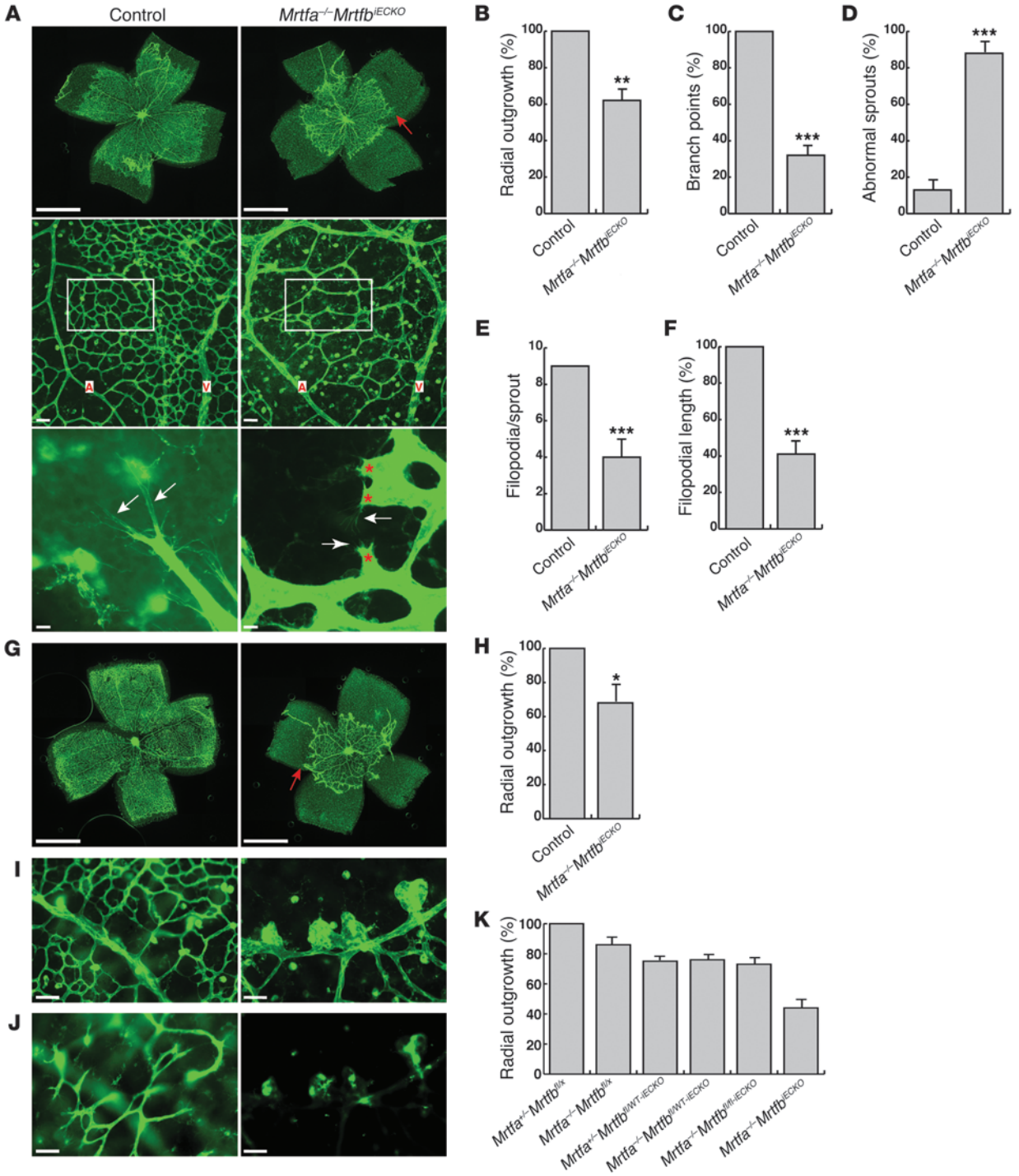

Figure 9

MRTF-A and MRTF-B are essential for retinal angiogenesis. (**A**) ILB4-staining on retinal flat-mounts of P6 control and *Mrtfa*$^{-/-}$*Mrtfb*^{iECKO} mice. Top: Progression of angiogenic front. Red arrow indicates recessed angiogenic front of primary plexus. Images are composites (see Methods). Middle: Vessel density between artery (A) and vein (V). Bottom: Sprout morphology. White arrows indicate filopodia; red asterisks indicate abnormal morphologies of *Mrtfa*$^{-/-}$*Mrtfb*^{iECKO} tip cells. (**B**–**D**) Quantitation of (**B**) percent radial outgrowth; (**C**) relative branch points in field of view (boxed regions in **A**, middle); and (**D**) abnormal sprouts. $n = 4$ (control); 6 (*Mrtfa*$^{-/-}$*Mrtfb*^{iECKO}). (**E** and **F**) Quantitation of (**E**) filopodia number per sprout and (**F**) filopodia mean length. $n = 54$ sprouts (control); 71 sprouts (*Mrtfa*$^{-/-}$*Mrtfb*^{iECKO}). (**G**) ILB4-stained retinal flat-mounts of P10 control and *Mrtfa*$^{-/-}$*Mrtfb*^{iECKO} retinae. Red arrow indicates recessed *Mrtfa*$^{-/-}$*Mrtfb*^{iECKO} angiogenic front. Images are composites (see Methods). (**H**) Percent radial outgrowth. $n = 9$ (control); 5 (*Mrtfa*$^{-/-}$*Mrtfb*^{iECKO}). (**I** and **J**) Higher-magnification views of (**I**) primary plexus and (**J**) deep plexi. (**K**) Percent radial outgrowth in P8 retinae, including all genotypes resulting from our mating scheme. $n = 8$ (*Mrtfa*$^{+/-}$*Mrtfb*$^{fl/x}$); 7 (*Mrtfa*$^{-/-}$*Mrtfb*$^{fl/x}$); 5 (*Mrtfa*$^{+/-}$*Mrtfb*$^{fl/WT\text{-}iECKO}$ and *Mrtfa*$^{+/-}$*Mrtfb*$^{fl/fl\text{-}iECKO}$); 6 (*Mrtfa*$^{-/-}$*Mrtfb*$^{fl/WT\text{-}iECKO}$ and *Mrtfa*$^{-/-}$*Mrtfb*^{iECKO}). See Supplemental Figure 3 for statistical comparisons. Scale bars: 1 mm (**A**, top, and **G**); 50 μm (**A**, middle, and **I** and **J**); 10 μm (**A**, bottom). $^{*}P < 0.05$, $^{**}P < 0.01$, $^{***}P < 0.001$ vs. respective control.

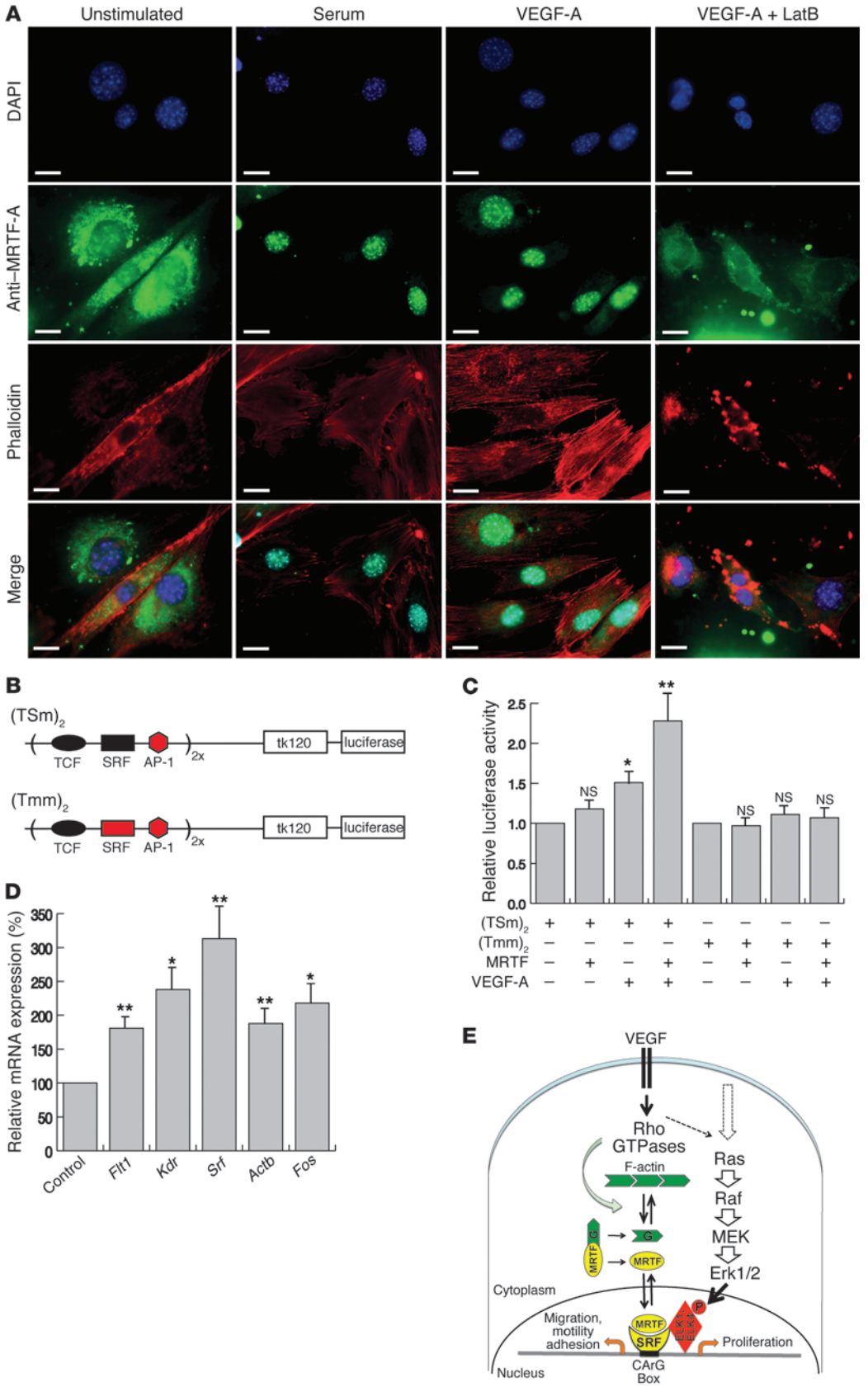

Figure 10

VEGF-A activates nuclear translocation of MRTF-A. (**A**) mECs were stimulated with serum, VEGF-A, or VEGF-A in the presence of latrunculin B (LatB) and stained for nuclei (DAPI; blue), MRTF-A (green), and F-actin (phalloidin; red). (**B**) Scheme of $(TSm)_2$ and $(Tmm)_2$ luciferase reporter constructs, which contain 2 tandem copies of the *c-Fos* SRE upstream of the thymidine kinase basal promoter sequence (tk120; –120 to +1), able to drive luciferase cDNA expression. (**C**) Relative luciferase activity in reporter-transfected HRMECs, with or without cotransfection of MRTF-A expression vectors and with or without VEGF-A stimulation. (**D**) Semiquantitative RT-PCR for genomic candidate mRNA expression in mECs upon VEGF-A treatment, expressed as percent untreated control. $n = 4$ (*Flt1*, *Srf*, and *Actb*); 3 (*Kdr* and *Fos*). (**E**) VEGF signaling leads to activation of the actin-MRTF-SRF axis. Note that interaction of MRTF and TCF cofactors (ELK1 and ELK4) with SRF is mutually exclusive. Scale bars: 10 μm (**A**). $^*P < 0.05$, $^{**}P < 0.01$ vs. respective control.

per field of view in an area between arteries and veins. Abnormal tip cells were defined as exhibiting stubby shafts with fewer and shorter filopodia. Abnormal sprouts along the angiogenic front were counted and expressed as a percentage of total sprouts. Numbers of filopodia per single sprout were averaged for control and mutant retinae.

Purification of ECs. P10 retinae were dissected and homogenized in 0.2% collagenase buffer at 37°C for 45 minutes. Cells were triturated using a 20-gauge syringe, passed through a 40-μm cell strainer, pelleted at 254 *g* for 5 minutes, and resuspended in serum-free HUVEC medium. ECs were bound to magnetic Dynabeads (Invitrogen) coated with anti-CD31 (BD Biosciences — Pharmingen) for 30 minutes at 4°C and separated magnetically from non-ECs.

RNA isolation, cDNA synthesis, and semiquantitative RT-PCR. Tissues were lysed for RNA isolation (Qiagen, RNeasy), cDNA was synthesized using random hexamers, and RT-PCR analysis was performed using specific primers (Purimex) and SYBR green technology (ABI Prism 7000 cycler) (55). See Supplemental Table 1 for primer sequences and amplification protocols.

Western blotting. Retinal tissue was lysed in Iyer buffer (56), and protein content was determined (Bradford reagent). Proteins were separated by SDS-PAGE in 4%–15% gradient gels. Electroblotting was at 4°C for 2 hours (100 V, 400 mA). Membranes were blocked in 10% milk powder (1 hour at room temperature). Primary antibody incubation was overnight at 4°C. After 3× washes with TST (Tris Saline Tween), membranes were incubated in secondary antibodies (1 hour at room temperature). Primary antibodies were as follows: GAPDH (1:20,000 dilution; Hytest Ltd.), VEGF-R2 (1:1,000 dilution; Cell Signaling), SRF (2C5, undiluted; ref. 57), P-cofilin (1:500 dilution; Cell Signaling). Secondary antibodies (all 1:10,000 dilution; all GE Healthcare) were anti-mouse, anti-rabbit, and anti-rat HRP. Band intensities were quantified densitometrically and normalized to GAPDH.

SLO and OCT. For SLO and OCT, mice were anesthetized by subcutaneous injection of ketamine (66.7 mg/kg) and xylazine (11.7 mg/kg). After anesthesia, pupils were dilated with tropicamide eye drops (Mydriaticum Stulln; Pharma Stulln). SLO imaging (58) was conducted with a Heidelberg Retina Angiograph (HRA I) equipped with an argon laser featuring 2 wavelengths (488 nm and 514 nm) in the short wavelength range and 2 infrared diode lasers (795 nm and 830 nm) in the long wavelength range. The fundus images presented here were recorded with the green laser (514 nm). Angiography was performed with 2 different dyes administered simultaneously: FLA at 488 nm (barrier filter 500 nm) and indocyanine green angiography (ICG) at 795 nm (barrier filter 800 nm). Dyes were given via subcutaneous injection of 75 mg/kg body weight fluorescein-Na (Tübingen University pharmacy), and 50 mg/kg body weight ICG (ICG-Pulsion; Pulsion Medical Systems AG). OCT was recorded with a Heidelberg Engineering Spectralis system with minor adaptations to the mouse eye as described previously (59).

Histological H&E and antibody staining. Eyes were fixed overnight at 4°C in Davidson fixative (6% formaldehyde, 32% EtOH, 11% acetic acid, 5% sucrose in PBS). 4-μm sections of paraffin-embedded eyes were mounted on Superfrost Plus slides and stained with H&E followed by dehydration and mounting in Entellan. For antibody staining, paraffin sections were blocked in 2% BSA/PBS-T for 1 hour at room temperature, followed by incubation with primary antibody overnight at 4°C. After washing 3× for 15 minutes with PBS-T, secondary antibodies were applied for 1 hour at room temperature. Cell nuclei were counterstained with DAPI. For microscopic analysis, sections were embedded in Mowiol.

Cell culture, transient transfection, and luciferase assay. Immortalized mECs (44) and HRMECs (Cell Systems) were cultured as recommended. Transient transfections used Promofectin (PromoCell). mECs were starved overnight and stimulated for 1 hour with either 15% FCS or 100 ng/ml VEGF-A. Pretreatment with latrunculin B was for 30 minutes. $(TSm)_2$ and $(Tmm)_2$ reporter plasmids (in which "m" denotes a mutated binding site) contained 2 tandem copies of the *c-Fos* serum response element (SRE) upstream of the thymidine kinase basal promoter sequence (–120 to +1), able to drive luciferase cDNA expression. The WT SRE contains binding sites for the transcription factors TCF, SRF, and AP-1. For transfection of siRNAs directed against *Srf* (siSRF797; Purimex) (60), mECs were seeded into 6-cm dishes with penicillin/streptomycin-free medium 1 day before transfection. For transfection (RNAiMAX reagent; Invitrogen) with 166 pmol siRNA per dish, cells had reached approximately 60% confluence. Transfection was stopped after 5 hours, and RNA was isolated 2 days later. Extracts for protein analysis were generated 2 and 3 days after transfection.

ChIP. For ChIP analysis (61), mECs were serum starved for 18 hours before stimulation with 15% FCS for 1 hour. See Supplemental Table 1 for primer sequences and amplification protocols. Anti-SRF ChIP signals of CArG boxes in *Actb* and *Thbs1* were normalized to either IgG-containing or no-antibody control reactions and expressed relative to *Pak1* (CArG box–negative control locus).

EM. For EM, retinae were fixed 4 hours in 2.5% glutaraldehyde (Paesel + Lorei GmbH) in 0.1 M cacodylate buffer (CB; pH 7.4). Specimens were washed in pure CB, postfixed in 1% OsO_4 in CB for 1 hour, dehydrated in ascending series of ethanol and propyleneoxide, bloc-stained in uranyl acetate for 4 hours, and flat-embedded in Araldite (Serva). An ultramicrotome (Ultracut; Leica) was used to cut semithin (1 μm) and ultrathin (50 nm) sections. Ultrathin sections were stained with lead citrate, mounted on copper grids, and analyzed with a Zeiss EM 10 electron microscope (Zeiss). Pictures were scanned at 300 dpi and processed (Adobe Photoshop).

Microscopy. Fluorescent staining analysis used inverse Zeiss Axiovert 200 M microscopes with AxioCam MRm camera and ApoTome (Zeiss), using AxioVision graphics software. Retinal overviews (original magnification, ×5) are presented as composite images of individual, successively overlapping (5%) images, generated by computer-controlled *x-y* settings and processed using MosaiX Software. H&E-stained sections were visualized using Zeiss Axioplan 2 with AxioCamHRc camera. Higher magnifications were obtained with ×10, ×20, ×40, and ×63 objectives.

Statistics. Data are presented as mean ± SEM. For comparisons between experiments, values were normalized to control (assigned as 1 or 100%). 2-tailed Student's *t* tests were used to identify statistical significance. Statistical significance was assumed for P values less than 0.05.

Study approval. All animal experiments were approved by the Regierungspräsidium Tübingen (Tübingen, Germany).

Acknowledgments

C. Weinl was supported by the Karl-Kuhn-Foundation, A. Nordheim was supported by the DFG (No120/12-4 and iRTG1302), and M.W. Seeliger was supported by the DFG (Se837/6-2) and the BMBF (grant 0314106). We thank Christina Seide for help with Figure 4 and Gabi Frommer-Kästle for skilful EM analysis.

Received for publication April 6, 2012, and accepted in revised form February 7, 2013.

Address correspondence to: Alfred Nordheim, Department for Molecular Biology, Interfaculty Institute of Cell Biology, Auf der Morgenstelle 15, University of Tübingen, 72076 Tübingen, Germany. Phone: 49.7071.297.8898; Fax: 49.7071.295.359; E-mail: alfred.nordheim@uni-tuebingen.de.

1. Adams RH, Alitalo K. Molecular regulation of angiogenesis and lymphangiogenesis. *Nat Rev Mol Cell Biol.* 2007;8(6):464–478.
2. Carmeliet P, Jain RK. Angiogenesis in cancer and other diseases. *Nature*. 2000;407(6801):249–257.
3. Ye X, Wang Y, Nathans J. The Norrin/Frizzled4 signaling pathway in retinal vascular development and disease. *Trends Mol Med.* 2010;16(9):417–425.
4. Sapieha P, et al. Retinopathy of prematurity: under-

standing ischemic retinal vasculopathies at an extreme of life. *J Clin Invest*. 2010;120(9):3022–3032.
5. Hammes HP, Feng Y, Pfister F, Brownlee M. Diabetic retinopathy: targeting vasoregression. *Diabetes*. 2011;60(1):9–16.
6. Ferris FL 3rd, Fine SL, Hyman L. Age-related macular degeneration and blindness due to neovascular maculopathy. *Arch Ophthalmol*. 1984;102(11):1640–1642.
7. Yannuzzi LA, et al. Retinal angiomatous proliferation in age-related macular degeneration. *Retina*. 2001;21(5):416–434.
8. Chew E, Gillies M, Bird A. Macular telangiectasia: a simplified classification. *Arch Ophthalmol*. 2006;124(4):573–574.
9. Dorrell MI, et al. Antioxidant or neurotrophic factor treatment preserves function in a mouse model of neovascularization-associated oxidative stress. *J Clin Invest*. 2009;119(3):611–623.
10. Yannuzzi LA, Bardal AM, Freund KB, Chen KJ, Eandi CM, Blodi B. Idiopathic macular telangiectasia. *Arch Ophthalmol*. 2006;124(4):450–460.
11. Gerhardt H, et al. VEGF guides angiogenic sprouting utilizing endothelial tip cell filopodia. *J Cell Biol*. 2003;161(6):1163–1177.
12. Bayless KJ, Johnson GA. Role of the cytoskeleton in formation and maintenance of angiogenic sprouts. *J Vasc Res*. 2011;48(5):369–385.
13. Jakobsson L, et al. Endothelial cells dynamically compete for the tip cell position during angiogenic sprouting. *Nat Cell Biol*. 2010;12(10):943–953.
14. Fruttiger M. Development of the mouse retinal vasculature: angiogenesis versus vasculogenesis. *Invest Ophthalmol Vis Sci*. 2002;43(2):522–527.
15. Claxton S, Kostourou V, Jadeja S, Chambon P, Hodivala-Dilke K, Fruttiger M. Efficient, inducible Cre-recombinase activation in vascular endothelium. *Genesis*. 2008;46(2):74–80.
16. Norman C, Runswick M, Pollock R, Treisman R. Isolation and properties of cDNA clones encoding SRF, a transcription factor that binds to the c-fos serum response element. *Cell*. 1988;55(6):989–1003.
17. Posern G, Treisman R. Actin' together: serum response factor, its cofactors and the link to signal transduction. *Trends Cell Biol*. 2006;16(11):588–596.
18. Buchwalter G, Gross C, Wasylyk B. Ets ternary complex transcription factors. *Gene*. 2004;324:1–14.
19. Shaw PE, Schroter H, Nordheim A. The ability of a ternary complex to form over the serum response element correlates with serum inducibility of the human c-fos promoter. *Cell*. 1989;56(4):563–572.
20. Selvaraj A, Prywes R. Megakaryoblastic leukemia-1/2, a transcriptional co-activator of serum response factor, is required for skeletal myogenic differentiation. *J Biol Chem*. 2003;278(43):41977–41987.
21. Wang DZ, et al. Potentiation of serum response factor activity by a family of myocardin-related transcription factors. *Proc Natl Acad Sci U S A*. 2002;99(23):14855–14860.
22. Pipes GC, Creemers EE, Olson EN. The myocardin family of transcriptional coactivators: versatile regulators of cell growth, migration, and myogenesis. *Genes Dev*. 2006;20(12):1545–1556.
23. Miralles F, Posern G, Zaromytidou AI, Treisman R. Actin dynamics control SRF activity by regulation of its coactivator MAL. *Cell*. 2003;113(3):329–342.
24. Vartiainen MK, Guettler S, Larijani B, Treisman R. Nuclear actin regulates dynamic subcellular localization and activity of the SRF cofactor MAL. *Science*. 2007;316(5832):1749–1752.
25. Mokalled MH, Johnson A, Kim Y, Oh J, Olson EN. Myocardin-related transcription factors regulate the Cdk5/Pctaire1 kinase cascade to control neurite outgrowth, neuronal migration and brain development. *Development*. 2010;137(14):2365–2374.
26. Miano JM. Role of serum response factor in the pathogenesis of disease. *Lab Invest*. 2010;90(9):1274–1284.
27. Olson EN, Nordheim A. Linking actin dynamics and gene transcription to drive cellular motile functions. *Nat Rev Mol Cell Biol*. 2010;11(5):353–365.
28. Gross C, Buchwalter G, Dubois-Pot H, Cler E, Zheng H, Wasylyk B. The ternary complex factor net is downregulated by hypoxia and regulates hypoxia-responsive genes. *Mol Cell Biol*. 2007;27(11):4133–4141.
29. Gross C, Dubois-Pot H, Wasylyk B. The ternary complex factor Net/Elk-3 participates in the transcriptional response to hypoxia and regulates HIF-1 alpha. *Oncogene*. 2008;27(9):1333–1341.
30. Chai J, Jones MK, Tarnawski AS. Serum response factor is a critical requirement for VEGF signaling in endothelial cells and VEGF-induced angiogenesis. *FASEB J*. 2004;18(11):1264–1266.
31. Franco CA, et al. Serum response factor is required for sprouting angiogenesis and vascular integrity. *Dev Cell*. 2008;15(3):448–461.
32. Holtz ML, Misra RP. Endothelial-specific ablation of serum response factor causes hemorrhaging, yolk sac vascular failure, and embryonic lethality. *BMC Dev Biol*. 2008;8:65.
33. Wang Y, et al. Ephrin-B2 controls VEGF-induced angiogenesis and lymphangiogenesis. *Nature*. 2010;465(7297):483–486.
34. Wiebel FF, Rennekampff V, Vintersten K, Nordheim A. Generation of mice carrying conditional knockout alleles for the transcription factor SRF. *Genesis*. 2002;32(2):124–126.
35. Muzumdar MD, Tasic B, Miyamichi K, Li L, Luo L. A global double-fluorescent Cre reporter mouse. *Genesis*. 2007;45(9):593–605.
36. Saint-Geniez M, D'Amore PA. Development and pathology of the hyaloid, choroidal and retinal vasculature. *Int J Dev Biol*. 2004;48(8–9):1045–1058.
37. Phng LK, et al. Nrarp coordinates endothelial Notch and Wnt signaling to control vessel density in angiogenesis. *Dev Cell*. 2009;16(1):70–82.
38. Mancuso MR, et al. Rapid vascular regrowth in tumors after reversal of VEGF inhibition. *J Clin Invest*. 2006;116(10):2610–2621.
39. Alberti S, et al. Neuronal migration in the murine rostral migratory stream requires serum response factor. *Proc Natl Acad Sci U S A*. 2005;102(17):6148–6153.
40. Heckenlively JR, et al. Mouse model of subretinal neovascularization with choroidal anastomosis. *Retina*. 2003;23(4):518–522.
41. Hu W, et al. Expression of VLDLR in the retina and evolution of subretinal neovascularization in the knockout mouse model's retinal angiomatous proliferation. *Invest Ophthalmol Vis Sci*. 2008;49(1):407–415.
42. Jiang A, Hu W, Meng H, Gao H, Qiao X. Loss of VLDL receptor activates retinal vascular endothelial cells and promotes angiogenesis. *Invest Ophthalmol Vis Sci*. 2009;50(2):844–850.
43. Xia CH, Lu E, Liu H, Du X, Beutler B, Gong X. The role of Vldlr in intraretinal angiogenesis in mice. *Invest Ophthalmol Vis Sci*. 2011;52(9):6572–6579.
44. Benedito R, et al. The notch ligands Dll4 and Jagged1 have opposing effects on angiogenesis. *Cell*. 2009;137(6):1124–1135.
45. Framson P, Bornstein P. A serum response element and a binding site for NF-Y mediate the serum response of the human thrombospondin 1 gene. *J Biol Chem*. 1993;268(7):4989–4996.
46. Costello P, Nicolas R, Willoughby J, Wasylyk B, Nordheim A, Treisman R. Ternary complex factors SAP-1 and Elk-1, but not net, are functionally equivalent in thymocyte development. *J Immunol*. 2010;185(2):1082–1092.
47. Berger W. Molecular dissection of Norrie disease. *Acta Anat (Basel)*. 1998;162(2–3):95–100.
48. Criswick VG, Schepens CL. Familial exudative vitreoretinopathy. *Am J Ophthalmol*. 1969;68(4):578–594.
49. Blake SM, et al. Thrombospondin-1 binds to ApoER2 and VLDL receptor and functions in postnatal neuronal migration. *EMBO J*. 2008;27(22):3069–3080.
50. Bornstein P. Thrombospondins function as regulators of angiogenesis. *J Cell Commun Signal*. 2009;3(3–4):189–200.
51. Oganesian A, Armstrong LC, Migliorini MM, Strickland DK, Bornstein P. Thrombospondins use the VLDL receptor and a nonapoptotic pathway to inhibit cell division in microvascular endothelial cells. *Mol Biol Cell*. 2008;19(2):563–571.
52. Yamauchi M, Imajoh-Ohmi S, Shibuya M. Novel antiangiogenic pathway of thrombospondin-1 mediated by suppression of the cell cycle. *Cancer Sci*. 2007;98(9):1491–1497.
53. Sakuma K, Akiho M, Nakashima H, Akima H, Yasuhara M. Age-related reductions in expression of serum response factor and myocardin-related transcription factor A in mouse skeletal muscles. *Biochim Biophys Acta*. 2008;1782(7–8):453–461.
54. Pitulescu ME, Schmidt I, Benedito R, Adams RH. Inducible gene targeting in the neonatal vasculature and analysis of retinal angiogenesis in mice. *Nat Protoc*. 2010;5(9):1518–1534.
55. Weinhold B, et al. Srf(–/–) ES cells display non-cell-autonomous impairment in mesodermal differentiation. *EMBO J*. 2000;19(21):5835–5844.
56. Iyer NV, et al. Cellular and developmental control of O_2 homeostasis by hypoxia-inducible factor 1 alpha. *Genes Dev*. 1998;12(2):149–162.
57. Koegel H, et al. Loss of serum response factor in keratinocytes results in hyperproliferative skin disease in mice. *J Clin Invest*. 2009;119(4):899–910.
58. Seeliger MW, et al. In vivo confocal imaging of the retina in animal models using scanning laser ophthalmoscopy. *Vision Res*. 2005;45(28):3512–3519.
59. Fischer MD, et al. Noninvasive, in vivo assessment of mouse retinal structure using optical coherence tomography. *PloS One*. 2009;4(10):e7507.
60. Werth D, et al. Proliferation of human primary vascular smooth muscle cells depends on serum response factor. *Eur J Cell Biol*. 2010;89(2–3):216–224.
61. Nelson JD, Denisenko O, Bomsztyk K. Protocol for the fast chromatin immunoprecipitation (ChIP) method. *Nat Protoc*. 2006;1(1):179–185.